RSC Advances

PAPER

View Article Online
View Journal | View Issue



Cite this: *RSC Adv.*, 2026, **16**, 16865

# Surface engineering of $SnO_2$ for improved perovskite/$SnO_2$ photodetectors

Jing Cai,[a] Guipeng Li,[b] Yulong Ying,[c] Hongping Li,*[d] Ahmad Fairuz Omar,[a] Marzaini Rashid*[a] and Mingming Chen*[b]

Received 31st December 2025
Accepted 20th March 2026

DOI: 10.1039/d5ra10121b

rsc.li/rsc-advances

Lead halide perovskite (LHP) heterojunctions have proven to be promising for achieving low-cost and efficient photodetection. However, the remarkable interfacial non-radiative recombination severely deteriorated the performance of the resulting devices. Herein, surface engineering of $SnO_2$ with ammonium tetrathiotungstate ($(NH_4)_2WS_4$) has been proposed to effectively passivate the interfacial defects at the LHP $CH_3NH_3PbI_3/SnO_2$ interface to fabricate high-performance photodetectors (PDs). Experimental and theoretical studies showed that the surface engineering with $(NH_4)_2WS_4$ resulted in S substituting for oxygen lattice of $SnO_2$, which passivated the surface oxygen vacancies of $SnO_2$. Further studies have shown that the S atoms at the surface of $SnO_2$ further suppressed the I vacancies and Pb vacancies at the bottom surface of $CH_3NH_3PbI_3$. Finally, improved $CH_3NH_3PbI_3/SnO_2$ PDs with the responsivity and detectivity of 0.41 A $W^{-1}$ and $5 \times 10^{12}$ Jones, respectively, at zero bias, have been demonstrated. The results presented in this work provide promising pathways to effectively passivate the interfacial defects of LHP/$SnO_2$ heterojunctions for achieving efficient photodetection in the future.



## Introduction

Photodetectors (PDs), which can directly convert photons into electrical charge, are a fundamental component of various modern photodetection and imaging systems, such as digital imaging and hyperspectral sensing.[1–5] Recently, halide lead perovskites (LHPs) ($ABX_3$, where A is $CH_3NH_3^+$ ($MA^+$), $HC(NH_2)_2^+$ ($FA^+$); B is the $Pb^{2-}$; X is the $Cl^-$, $Br^-$, and $I^-$) have attracted tremendous attention in the optoelectronics community because of their superior optoelectrical properties including high absorption coefficient, long charge carrier diffusion length, and long charge carrier lifetime.[6] Benefiting from these advantages, LHPs have been regarded as potential candidates for realizing low-cost and efficient light harvesting and photodetection.[7] Notably, various kinds of LHP PDs, including narrowband, broadband, and wavelength-selective PDs, have been fabricated recently.[8,9] Benefiting from various advantages, such as a combination of optoelectrical properties of both semiconductors and being free from the need for controlled n- and p-type doping of specific materials,[10–13] LHP heterojunctions fabricated by preparing LHP and a different semiconductor in sequence have been considered as essential building blocks for fabricating efficient and cost-effective self-powered PDs.[14,15]

Recently, the rapid progresses of power conversion efficiency of LHP solar cells have motivated the explorations of advanced carrier transport layers.[16] It is worth noting that wide bandgap semiconductor tin oxide ($SnO_2$) has been widely employed to fabricate efficient LHP solar cells recently, benefiting from its high electron mobility, deep conduction band, and low-temperature processabilities.[17] Meanwhile, the construction of efficient PDs based on various LHP/$SnO_2$ heterojunctions has been further explored.[18] Similar to light harvesting, efficient photodetection can be readily achieved through a combination of the efficient absorption of photons and the efficient collection of excess carriers. Benefiting from ion doping-assisted suppression of point defects and seed layer-assisted nucleation-induced suppression of grain defects, the bulk defects of LHP thin films have been remarkably suppressed.[19,20] However, the interfacial defects induced non-radiative recombination have severely lowered the efficiency of carrier collection, greatly limiting the performance of LHP/$SnO_2$ heterojunction PDs.[21,22] In general, the interfacial defects consist of the surface defects of the buried layer and the deposited layer. In the case of the LHP/$SnO_2$ heterojunctions, the $SnO_2$ thin films prepared with various techniques have suffered from the natural surface oxygen vacancies ($V_O$s).[22] In addition, halide vacancies and lead vacancies have been evidenced at the bottom surface of LHPs owing to the weak bonding between LHPs and $SnO_2$.[23] It has been widely reported

[a]*School of Physics, Universiti Sains Malaysia, 11800 USM, Penang, Malaysia. E-mail: marzaini@usm.my*

[b]*Department of Microelectronics, Jiangsu University, Zhenjiang, Jiangsu 212013, China. E-mail: andychain@live.cn*

[c]*School of Materials Science and Engineering, Zhejiang Sci-Tech University, Hangzhou, 310018, China*

[d]*School of Materials Science and Engineering, Jiangsu University, Zhenjiang, Jiangsu 212013, China. E-mail: hpli@ujs.edu.cn*

that both surface defects deteriorated the performance of LHP/$SnO_2$ heterojunction devices.[24] Very recently, a great amount of effort has been devoted to suppressing the interfacial defects for fabricating improved LHP/$SnO_2$ heterojunction PDs.[25] However, the existing literatures mostly focused on either passivating the surface $V_O$s of $SnO_2$ thin films or suppressing the halide vacancies and lead vacancies at the bottom surface of LHPs.[26,27] For example, inorganic dielectric layers have been employed to passivate the surface $V_O$s of $SnO_2$ thin films.[28] Besides, various organic groups have been explored, but mainly suppress the halide vacancies and lead vacancies at the bottom surface of LHP thin films.[29] Practically, effective suppression of surface defects of both materials is fundamental for improving the performance of LHP/$SnO_2$ heterojunction PDs, while the related studies have seldom been reported so far.

Herein, surface engineering of $SnO_2$ with ammonium tetrathiotungstate ($(NH_4)_2WS_4$) has been proposed to realize an effective suppression of surface $V_O$s of $SnO_2$ and iodine vacancies ($V_I$) and lead vacancies ($V_{Pb}$) at the bottom surface of $MAPbI_3$. It has been shown that the surface $V_O$s of $SnO_2$ were effectively passivated *via* the sulfur (S) substitution for oxygen (O) lattice. In addition, the S atoms at the surface of $SnO_2$ further suppressed the $V_I$ and $V_{Pb}$ defects at the bottom surface of $MAPbI_3$. Collectively, performance-improved $MAPbI_3$/$SnO_2$ PDs with the responsivity and detectivity as high as 0.41 A $W^{-1}$ and $5 \times 10^{12}$ Jones, respectively, at the zero bias, have been demonstrated.

## Results and discussions

The $MAPbI_3$/$SnO_2$ PDs were fabricated by spin-coating $SnO_2$ and $MAPbI_3$ thin films in sequence on an ITO substrate (Fig. 1a) (see experiments in SI for details). The treatment of surface engineering of $SnO_2$ was realized by adding $(NH_4)_2WS_4$ into $SnO_2$ aqueous solution, where the surface $V_O$s of $SnO_2$ were passivated through the S substitution during stirring. The morphological and structural properties of samples were characterized by scanning electron microscopy (SEM) and X-ray diffraction (XRD) techniques. The suppression of surface $V_O$ defects in $SnO_2$ and $V_{Pb}$ of $MAPbI_3$ has been verified through steady-state and transient photoluminescence (PL), X-ray photoelectron spectroscopy (XPS) characterizations, and density functional theory (DFT) calculations.

Structure and elements analysis have confirmed the crystallization of $SnO_2$ after spin-coating of pure $SnO_2$ and $SnO_2$/$(NH_4)_2WS_4$ aqueous solutions (Fig. S1–S2, SI). Fig. 1b and c show the typical SEM images of $SnO_2$ and S-$SnO_2$ thin films. It shows that the S-$SnO_2$ thin films exhibit an improved morphology in terms of improved compactness and uniformity, while the $SnO_2$ thin films show a rough surface with notable gaps. This suggests that the $(NH_4)_2WS_4$ additive benefits the preparation of high-quality $SnO_2$ thin films from nanoparticles. Due to the small thickness and limited resolution of the SEM technique, the thickness of $SnO_2$ and S-$SnO_2$ thin films was not obtained, but has been estimated as ~10 nm from the previous reports.[30] Notably, the compact and uniform morphology of S-$SnO_2$ thin films exhibits a reduction of carrier scattering effect. As revealed from current–voltage (*I–V*) measurements (Fig. S3, SI), the S-$SnO_2$ thin films feature a reduced resistivity. As a result, the carrier collection at the $MAPbI_3$/$SnO_2$ interfaces is expected to be improved.

Fig. 1d–g present the SEM images of $MAPbI_3$ thin films spin-coated on $SnO_2$ and S-$SnO_2$ thin films. As shown, both samples exhibit a similar morphology with comparable grain size, compactness, and thickness. Specifically, the grain sizes and thickness of both samples were characterized as around 450 ± 32 nm (Fig. 1d and e) and 230 nm (Fig. 1f and g), respectively. This suggests that surface engineering of $SnO_2$ with $(NH_4)_2WS_4$ seems not to influence the growth processes of $MAPbI_3$ thin films.

Structural and optical properties measurements were carried out to further compare the quality of $MAPbI_3$ thin films prepared on $SnO_2$ and S-$SnO_2$ thin films, and the results are shown in Fig. 2. It shows that both $MAPbI_3$ thin films exhibit similar XRD patterns (Fig. 2a), which can be indexed into the orthorhombic phase. Careful analysis shows that both $MAPbI_3$ thin films exhibit similar crystalline quality from the XRD peaks' positions and full width at half maximums (FWHMs, Table S1, SI). Such a claim can be supported from small differences in their steady and transient PL spectra (Fig. 2b). As shown, the PL intensity and carrier recombination processes of both $MAPbI_3$ thin films are almost same. Collectively, surface engineering with the $(NH_4)_2WS_4$ has improved the morphology of $SnO_2$ thin films, while it has neglected roles in subsequent crystallization of $MAPbI_3$ thin films.

To verify the suppression of surface $V_O$s, XPS measurements on the $SnO_2$ thin films were performed. Notably, the XPS method has shown strong effectiveness in analyzing surface chemical composition.[31,32] Fig. 3a illustrates the core-level spectra of O 1s of $SnO_2$ and S-$SnO_2$ thin films. Both spectra can be fitted into three peaks (peak I, II, and III), which correspond to various states of O at the $SnO_2$ surface. As can be seen, the binding energies are observed at 530.5 eV, 531.3 eV, and 532.0 eV, which can be attributed to lattice O, $V_O$, and adsorbed oxhydryl ($OH^-$), respectively.[33] Notably, the concentration of various components can be semiquantitatively evaluated from the relative intensities of corresponding XPS peaks.[33] Accordingly, it can be concluded that S-$SnO_2$ thin films show a reduced surface $V_O$ from the decreased intensity of peak II compared to $SnO_2$ thin films. Further observations suggest that the reduction of surface $V_O$s is probably caused by the S substituting for O in S-$SnO_2$ thin films. On the one hand, a remarkable peak can be observed in S 2p XPS spectrum (Fig. 3b), which verifies the successful doping of S in S-$SnO_2$ thin films. On the other hand, the binding energies of Sn 3d in S-$SnO_2$ thin films redshift by around 0.3 eV compared to those in $SnO_2$ thin films (Fig. 3c). This is attributed to the increased electron density around Sn atoms,[34] which well correlates to the formation of the Sn–S bond in the current situation.

The above observations indicate that interface engineering with $(NH_4)_2WS_4$ resulted in a doping of S atoms, which suppressed the surface $V_O$s in S-$SnO_2$ thin films. However, it is difficult to reveal the doping processes at this stage, but can be expected as follows:

 

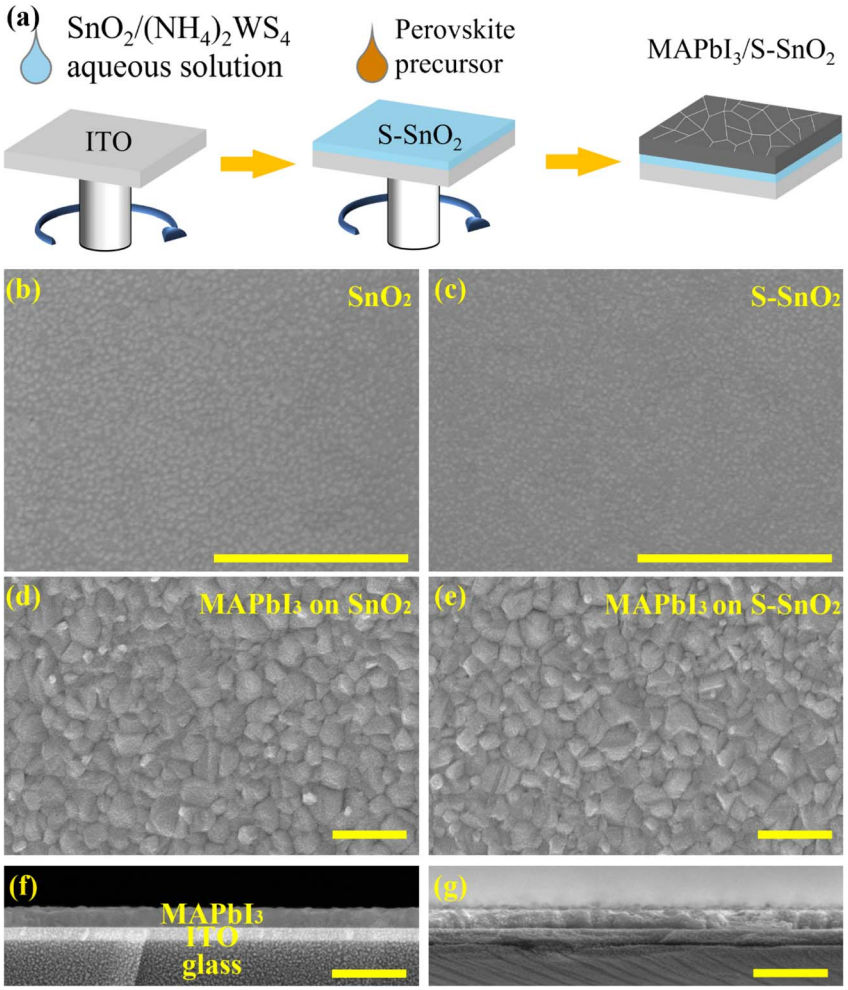


Fig. 1 Morphology of $SnO_2$ and $MAPbI_3$ thin films. (a) Scheme of experimental details for preparing $MAPbI_3$/S-$SnO_2$ heterojunctions. SEM images of (b) $SnO_2$, (c) S-$SnO_2$, (d and f) $MAPbI_3$ thin films grown on $SnO_2$, and (e and g) $MAPbI_3$ thin films grown on S-$SnO_2$.

$$SnO_2\_V_O + S \rightarrow SnO_2\_S_O$$

where $SnO_2\_V_O$ is the $SnO_2$ with a surface $V_O$, $SnO_2\_S_O$ is the $SnO_2$ with S substituting for O lattice. Herein, to better understand the mechanisms of suppression of surface $V_O$s by S doping, DFT calculations were carried out. As reported before, the probability of S substitution for surface O lattice ($S_O$) can be revealed from their formation energies ($\Delta E$),[35] which can be calculated from the eqn (1):

$$\Delta E(SnO_2\_S_O) = E(SnO_2\_S_O) - [E(SnO_2\_V_O) + E(S)] \quad (1)$$

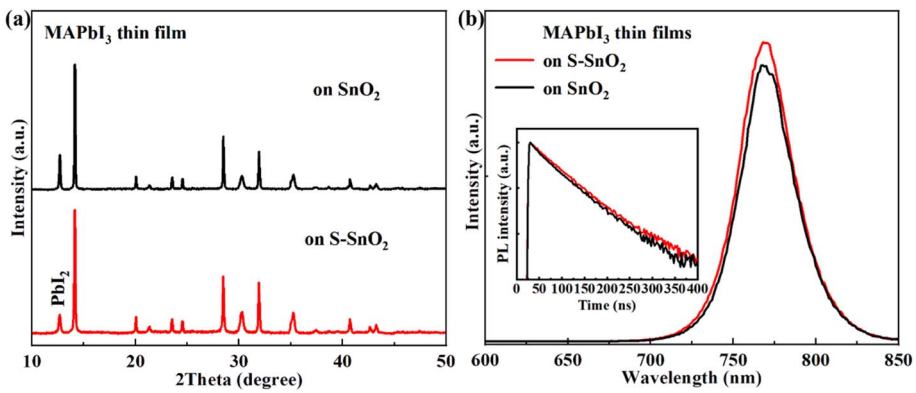


Fig. 2 Structural and optical properties of $MAPbI_3$ thin films grown on $SnO_2$ and S-$SnO_2$. (a) XRD and (b) PL. The inset in (b) shows the TRPL.

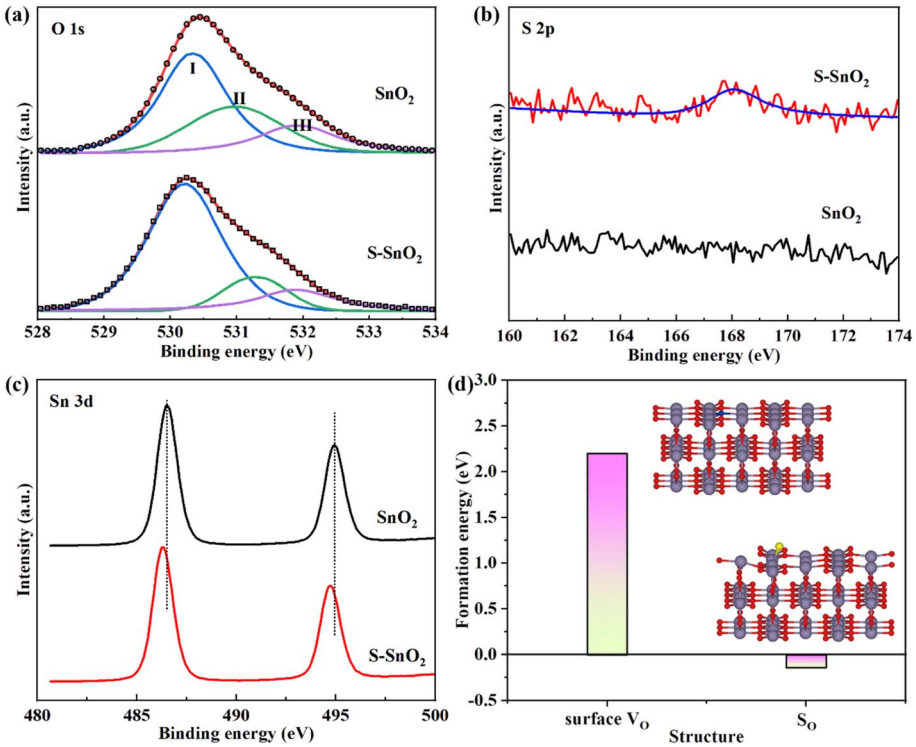


Fig. 3 Passivation of surface $V_O$s of $SnO_2$ by S atoms. (a–c) XPS data of (a) O, (b) S, and (c) Sn atoms. (d) Formation energies of surface $V_O$s and S substituting for O of $SnO_2$. The inset in (d) indicates the corresponding supercells, where red, gray, blue, and yellow balls are O, Sn, $V_O$, and S, respectively.

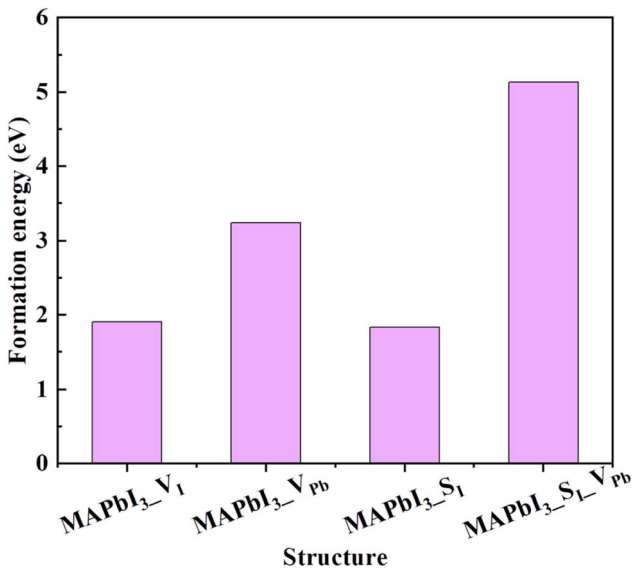


Fig. 4 Formation energies of $V_I$, $V_{Pb}$, S substituting for I, and S substituting for I with a $V_{Pb}$ nearby of $MAPbI_3$. The corresponding supercells are depicted in Fig. S4 (SI). The formation energies were calculated using formulas similar to eqn (1).

where $E(SnO_2\_S_O)$, $E(SnO_2\_V_O)$, and $E(S)$ are the total energies of the supercell with S substitution for surface O and that with a surface $V_O$, and the energy of individual S atom, respectively. The formation energy of $SnO_2\_V_O$ structure ($\Delta E(SnO_2\_V_O)$) was calculated with a similar scenario. Fig. 3d depicts the formation energies of $SnO_2$ with a surface $V_O$ and S substitution for surface O. It can be seen that the formation energy of surface $V_O$ is as high as 2.198 eV. This suggests that the high-density surface $V_O$ (Fig. 3a) cannot be related to thermodynamic effects, but might be attributed to mechanical effects between the nanoparticles or hydrogen bonding in the solvent environment. Notably, the formation energy of S substitution for surface O was calculated as low as −0.141 eV. This shows that the $S_O$ structure is thermally preferred, which demonstrates the effective suppression of surface $V_O$s of $SnO_2$ through the surface engineering with the $(NH_4)_2WS_4$.

It has been noticed that S atoms on the $SnO_2$ surface showed a strong electrostatic interaction with Pb ions of $MAPbI_3$ compared to O of $SnO_2$.[36] In this case, the interfacial S atoms are expected to fill the $V_I$ and further suppress the formation of $V_{Pb}$ at the bottom surface of $MAPbI_3$ thin films. Since the small penetration depth of X-ray, the local chemical states of Pb and I atoms at the $MAPbI_3/SnO_2$ interface cannot be experimentally explored from XPS techniques. To demonstrate the hypotheses, the formation energies of $MAPbI_3$ with a $V_I$ ($MAPbI_3\_V_I$), $MAPbI_3$ with a $V_{Pb}$ ($MAPbI_3\_V_{Pb}$), $MAPbI_3$ with a S atom substituting for I lattice ($MAPbI_3\_S_I$), and $MAPbI_3\_S_I$ with a $V_{Pb}$ nearby S ($MAPbI_3\_S_I\_V_{Pb}$) (Fig. S4, SI) were calculated, and the results are provided in Fig. 4. It shows that the $MAPbI_3\_S_I$ structure shows a reduced formation energy (1.84 eV) compared to $MAPbI_3\_V_I$ (1.91 eV), and the $MAPbI_3\_S_I\_V_{Pb}$ exhibits a reduced formation energy (3.25 eV) compared to $MAPbI_3\_V_{Pb}$

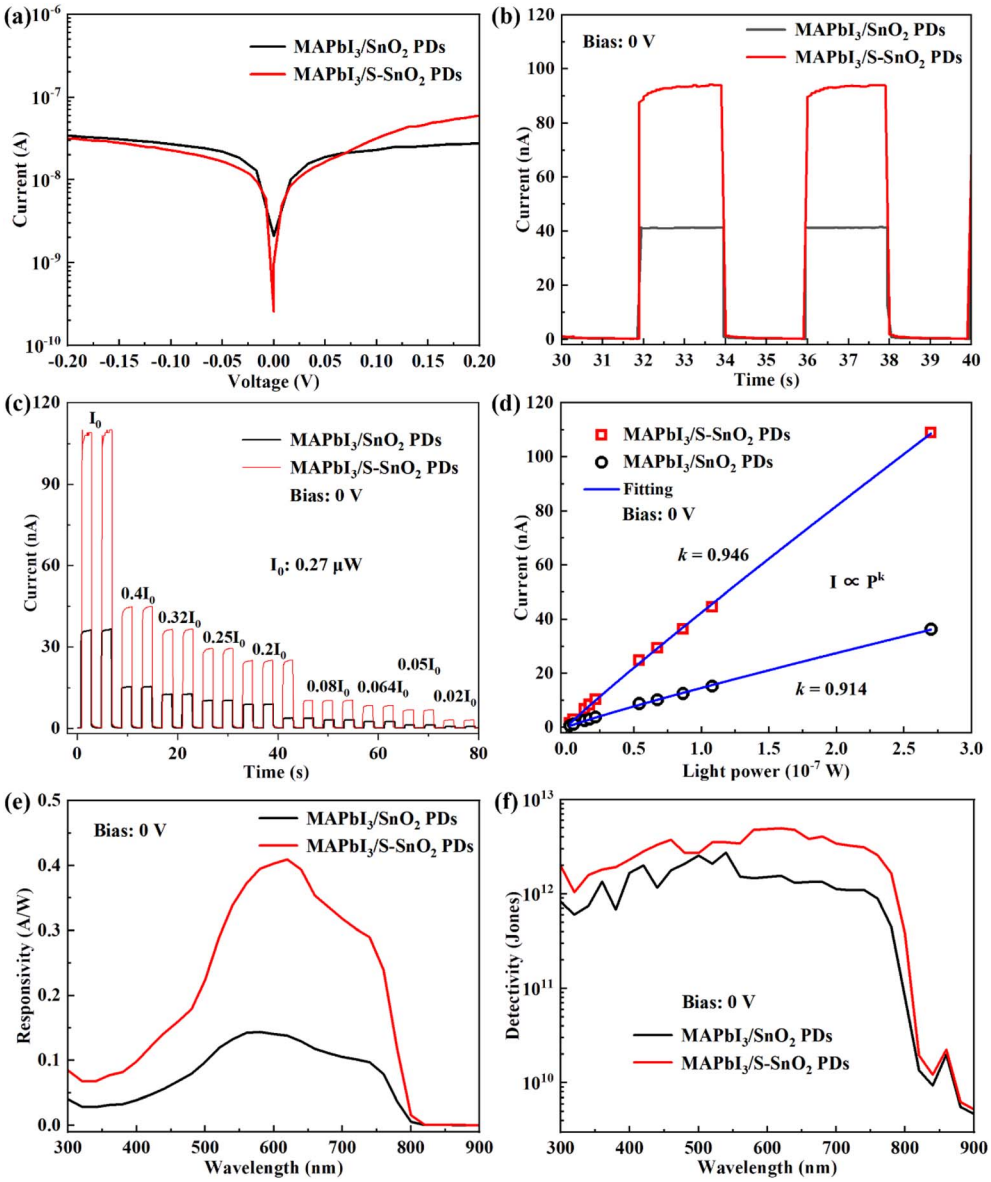


Fig. 5 Performance of $MAPbI_3/SnO_2$ PDs. (a) *I*–*V* curves captured in dark. (b) *I*–*t* curves captured under pulsed illumination. (b and c) *I*–*t* curves and photocurrent captured under different light powers. Data in d were extracted from c. (e) Responsivity. (f) Detectivity.

(5.14 eV). This suggests that the S atoms at the surface of $SnO_2$ thin films have remarkable potential to suppress the $V_I$ and $V_{Pb}$ defects at the bottom surface of $MAPbI_3$ thin films.

After sputtering Au electrodes, $MAPbI_3/SnO_2$ heterojunction PDs were fabricated (Fig. S5, SI). As shown in Fig. S6 (SI), among various concentrations, engineering $SnO_2$ NPs with 1.0 mg $mL^{-1}$ of $(NH_4)_2WS_4$ produced the optimal $MAPbI_3$/S-$SnO_2$ PDs, resulting in the highest photocurrent. Accordingly, the performance of $MAPbI_3$/S-$SnO_2$ PDs, prepared with 1.0 mg $mL^{-1}$ $(NH_4)_2WS_4$ engineering, is examined in detail below. Fig. 5a illustrates the *I*–*V* curves of $MAPbI_3/SnO_2$ and $MAPbI_3$/S-$SnO_2$ PDs captured in the dark. It shows that the $MAPbI_3$/S-$SnO_2$ PDs exhibit reduced current under reverse bias and reduced turn-on voltage under forward bias. As shown in Fig. 1 and 2, the $MAPbI_3$ thin films prepared on $SnO_2$ and S-$SnO_2$ exhibit a similar crystalline quality. Thus, the reduced reverse current and turn-on voltage can be attributed to the suppression of interfacial defects at the $MAPbI_3$/S-$SnO_2$ interface, as discussed above.

Fig. 5b shows the current–time (*I*–*t*) curves of $MAPbI_3/SnO_2$ and $MAPbI_3$/S-$SnO_2$ PDs at zero bias with 540 nm illumination switched on and off. It can be seen that both devices show excellent on-off switching performance. Notably, the $MAPbI_3$/S-$SnO_2$ PDs show an improved photocurrent, which increased by around 2.2 times compared to $MAPbI_3/SnO_2$ PDs. According to above discussions, this should be caused by the suppressed interfacial non-radiative recombination at $MAPbI_3$/S-$SnO_2$ interfaces. Further studies suggest that both devices exhibit nearly a linear response to light power. As shown in Fig. 5c and d, the photocurrents of $MAPbI_3/SnO_2$ and $MAPbI_3$/S-$SnO_2$ PDs nearly scale linearly with light power from $10^{-9}$ W to $10^{-7}$ W,

Table 1 Comparison of photodetection performance of $MAPbI_3/SnO_2$ heterojunction PDs and related devices reported before

| Device | Bias (V) | Responsivity (A/W) | Detectivity (Jones) | Ref. |
|---|---|---|---|---|
| Spiro-OMeTAD/$FAPb(I/Br)_3/SnO_2$ | 1.0 | 0.0438 | $3.56 \times 10^{13}$ | 37 |
| Spiro-OMeTAD/$MAFAPb(Br/I)_3/SnO_2$ | 1.0 | 0.0722 | $4.67 \times 10^{13}$ | 38 |
| $SnO_2/MAPbI_3/MoO_3$ | 0 | 0.0509 | $2.23 \times 10^{12}$ | 39 |
| $CsCu_2I_3$/GaN | 0 | 0.10634 | $9.24 \times 10^{11}$ | 40 |
| $MAPbI_3$/ZnO | 7 | 2.73 | $1.09 \times 10^{12}$ | 41 |
| $C_{60}/MAPbI_3$/GaN | 0 | 0.198 | $7.96 \times 10^{12}$ | 42 |
| $TiO_2/MAPbI_3$ | −0.8 | 0.405 | $2.07 \times 10^{11}$ | 43 |
| PEDOT:PSS/$MAPbI_3$/PTB7-Th:COTIC-4F | −0.5 | 0.58 | $1.64 \times 10^{12}$ | 44 |
| $MAPbI_3/SnO_2$@r-$PMo_{11}V$ | 3 | 0.039 | $9.3 \times 10^{10}$ | 45 |
| $MAPbI_3$/S-$SnO_2$ | 0 | 0.41 | $4.6 \times 10^{12}$ | This work |

suggesting that $MAPbI_3/SnO_2$ heterojunction PDs can be used to detect the light power.

The performance of $MAPbI_3/SnO_2$ and $MAPbI_3$/S-$SnO_2$ PDs is further studied from the responsivity and detectivity, and the results are shown in Fig. 5c and d. As reported before, the responsivity ($R$) and detectivity ($D^*$) can be calculated from eqn (2) and (3) provided below:

$$R = \frac{I_{ph} - I_{dark}}{P \times S} \quad (2)$$

$$D^* = \frac{R}{\sqrt{2eI_{dark}/S}} \quad (3)$$

where $I_{ph}$ and $I_{dark}$ are the photocurrent and dark current, $P$ is the light power density (in W $cm^{-2}$), $S$ is the device area (the area of the top Au electrode, 0.01 $mm^2$), $e$ is the electric charge ($1.6 \times 10^{-19}$ C). As depicted in Fig. 5e and f, the photoresponsivity and detectivity of $MAPbI_3/SnO_2$ PDs are 0.14 A $W^{-1}$ and $2 \times 10^{12}$ Jones, respectively, at the zero bias, which increased by around 2.9 times (0.41 A $W^{-1}$) and 2.3 times ($4.6 \times 10^{12}$ Jones) for $MAPbI_3$/S-$SnO_2$ PDs. The improved photodetection performance of $MAPbI_3$/S-$SnO_2$ PDs is mainly attributed to the suppressed interfacial non-radiative recombination, which benefits from the effective interfacial passivation induced by the surface engineering with $(NH_4)_2WS_4$ as evidenced above. Table 1 summarizes a comparison of the photodetection performance of the $MAPbI_3$/S-$SnO_2$ PDs shown herein and related PDs reported before, highlighting the critical roles of surface engineering with $(NH_4)_2WS_4$ in improving the performance of $MAPbI_3/SnO_2$ heterojunction PDs.

Further studies reveal that surface engineering of $SnO_2$ with $(NH_4)_2WS_4$ improved the stability of photodetection. As shown in Fig. 6a and b, the photocurrent of $MAPbI_3/SnO_2$ PDs decreases to 85% of the initial value under pulsed illumination (Fig. 6a) and 60% under steady illumination (Fig. 6b) over 3600 s. In comparison, the photocurrent slightly decreases (2% and 10%) in $MAPbI_3$/S-$SnO_2$ PDs. Generally, the interfacial non-radiative recombination induces substantial thermal effects under illumination,[46] which account for the inferior stability observed in $MAPbI_3/SnO_2$ PDs. Thus, the improved stability of photodetection of $MAPbI_3$/S-$SnO_2$ mainly benefits from the effective interfacial passivation as discussed above.

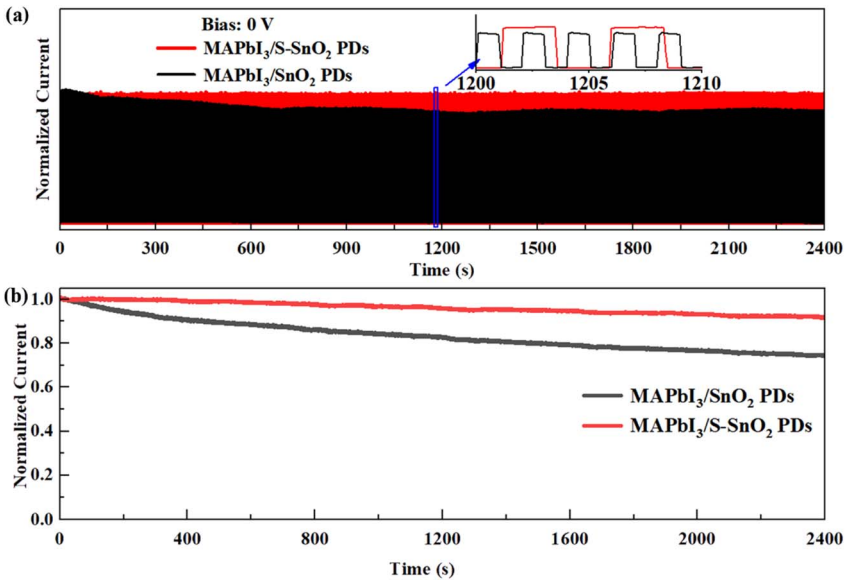


Fig. 6 Stability of photodetection of $MAPbI_3/SnO_2$ PDs. $I$–$t$ curves captured (a) under pulsed illumination and (b) steady illumination.

In conclusion, surface engineering of $SnO_2$ with $(NH_4)_2WS_4$ has been demonstrated to effectively passivate the interfacial defects to fabricate improved $MAPbI_3/SnO_2$ PDs. It has been shown that the surface engineering with $(NH_4)_2WS_4$ resulted in S substituting for O lattice of $SnO_2$, which passivated the surface $V_O$s of $SnO_2$. Meanwhile, theoretical studies suggested that the S atoms at the surface of $SnO_2$ further suppressed the $V_I$ and $V_{Pb}$ at the bottom surface of $MAPbI_3$. Accordingly, the interfacial non-radiative recombination has been suppressed. On this basis, improved $MAPbI_3/SnO_2$ PDs have been fabricated, where the responsivity and detectivity of 0.41 A $W^{-1}$ and $5 \times 10^{12}$ Jones at the zero bias have been demonstrated. The results shown in this work pave the way for efficiently passivating the interfacial defects of LHP/$SnO_2$ heterojunctions in the future.

## Conflicts of interest

The authors declare no conflict of interest.

## Data availability

The data that support the findings of this study are available from the corresponding authors upon reasonable request.

Supplementary information (SI): experiments, and supporting figures including XRD and XPS results of $SnO_2$ and S-$SnO_2$ thin films, *I–V* curves of Au/$SnO_2$ (S-$SnO_2$)/ITO structures, supercells of $MAPbI_3$ containing various defects, and a photo image of $MAPbI_3/SnO_2$ PDs, statistical results of dark current and photocurrent of $MAPbI_3/SnO_2$ PDs treated with different $(NH_4)_2WS_4$, and supporting Tables for comparison of crystallinity of $MAPbI_3$ thin films prepared on $SnO_2$ and S-$SnO_2$. See DOI: https://doi.org/10.1039/d5ra10121b.

## References

1 U. Khulal, J. Zhao, W. Hu and Q. Chen, Nondestructive quantifying total volatile basic nitrogen (TVB-N) content in chicken using hyperspectral imaging (HSI) technique combined with different data dimension reduction algorithms, *Food Chem.*, 2016, **197**, 1191–1199.
2 J. Sun, S. Jiang, H. Mao, X. Wu and Q. Li, Classification of Black Beans Using Visible and Near Infrared Hyperspectral Imaging, *Int. J. Food Prop.*, 2016, **19**(8), 1687–1695.
3 Q. Chen, W. Hu, J. Su, H. Li, Q. Ouyang and J. Zhao, Nondestructively sensing of total viable count (TVC) in chicken using an artificial olfaction system based colorimetric sensor array, *J. Food Eng.*, 2016, **168**, 259–266.
4 L. Wan, H. Li, C. Li, A. Wang, Y. Yang and P. Wang, Hyperspectral Sensing of Plant Diseases: Principle and Methods, *Agronomy*, 2022, **12**(6), 1451.
5 Y. Xu, M. M. Hassan, A. S. Sharma, H. Li and Q. Chen, Recent advancement in nano-optical strategies for detection of pathogenic bacteria and their metabolites in food safety, *Crit. Rev. Food Sci. Nutr.*, 2023, **63**(4), 486–504.
6 R. Wang, M. Mujahid, Y. Duan, Z.-K. Wang, J. Xue and Y. Yang, A Review of Perovskites Solar Cell Stability, *Adv. Funct. Mater.*, 2019, **29**(47), 1808843.
7 Z. Y. Zhang, L. Sun and G. P. Wang, Lateral Perovskite Single-Crystal Capacitors for Self-Powered Photodetection, *Adv. Electron. Mater.*, 2023, **9**(4), 2201318.
8 X. Shen, S. Yang, M. Chen, J. Su, J. Cai, P. Cheng, Y. Liu, Q. Wang and D. Cao, Interfacial Engineering with Aluminum Oxide toward an Improved Self-Powered Narrowband Visible-Light Photodetection in Lead Halide Perovskite $CH_3NH_3PbBr_3$/p-Si Heterojunctions, *Adv. Mater. Interfaces*, 2022, **9**(14), 2102305.
9 L.-J. Feng, Y.-Y. Zhao, R.-Y. Song and X.-W. Lei, Three homologous 1D lead halide perovskites with broadband white-light emissions, *Inorg. Chem. Commun.*, 2022, **136**, 109146.
10 P. C. Kumar, S. Mohanty, J. Panda, S. Das, S. Supriya, D. Alagarasan and R. Naik, Enhanced photoresponse in a Ag2S/In2Se3 heterojunction based visible light photodetector, *RSC Adv.*, 2025, **15**(18), 14518–14531.
11 L. Mahapatra, S. Supriya, P. C. Kumar, D. Alagarasan, C. Sripan and R. Naik, Increase in photo sensitivity and detectivity of Bi/Sb35S35Se30 heterostructure films upon time-dependent laser irradiation for photodetection, *Surf. Interfaces*, 2025, **72**, 107091.
12 K. Manjunatha, D. Alagarasan, S. Das, R. Ganesan, R. Naik, D. Purohit and M. Ramudu, Influence of substrate temperature on SnSe2/TiO2 heterostructure for photodetector applications, *Sens. Actuators, A*, 2025, **391**, 116641.
13 G. Mallick, P. C. Kumar, R. Naik and R. Biswal, Enhanced Photoresponse from Ag/Bi2Se3 Heterostructure Thin Films under Thermal Annealing, *ACS Appl. Electron. Mater.*, 2025, **7**(12), 5583–5598.
14 S. Kumaresan, I. Kathiravan, V. Vijendran and J. Balasundaram, Inorganic hole transport layer for lead free bismuth halide perovskite for photovoltaic device, *Opt. Mater.*, 2024, **154**, 115722.
15 J. Haddad, B. Krogmeier, B. Klingebiel, L. Krueckemeier, S. Melhem, Z. Liu, J. Huepkes, S. Mathur and T. Kirchartz, Analyzing Interface Recombination in Lead-Halide Perovskite Solar Cells with Organic and Inorganic Hole-Transport Layers, *Adv. Mater. Interfaces*, 2020, **7**(16), 2000366.
16 K. Ahmad and R. A. Khan, Improved photovoltaic performance of lead halide perovskite solar cells using spiro-OMeTAD plus CNTs as hole transport layer, *J. Mater. Sci. Mater. Electron.*, 2025, **36**(7), 425.
17 J. Kim, K. S. Kim and C. W. Myung, Efficient electron extraction of $SnO_2$ electron transport layer for lead halide perovskite solar cell, *npj Comput. Mater.*, 2020, **6**(1), 100.
18 L. Huang, X. Sun, C. Li, J. Xu, R. Xu, Y. Du, J. Ni, H. Cai, J. Li, Z. Hu and J. Zhang, UV-Sintered Low-Temperature Solution-Processed $SnO_2$ as Robust Electron Transport Layer for Efficient Planar Heterojunction Perovskite Solar Cells, *ACS Appl. Mater. Interfaces*, 2017, **9**(26), 21909–21920.
19 Z. Molenda, S. Chambon, D. M. Bassani and L. Hirsch, Electronic Doping in Perovskite Solar Cells, *Adv. Electron. Mater.*, 2024, **10**(10), 2400090.

20 J. Jeong, H.-B. Kim, Y. J. Yoon, N. G. An, S. Song, J. W. Kim, M. Kim, H. Jang, D. S. Kim, G.-H. Kim and J. Y. Kim, The introduction of a perovskite seed layer for high performance perovskite solar cells, *J. Mater. Chem. A*, 2018, **6**(41), 20138–20144.

21 X. Meng, J. Deng, Q. Sun, B. Zong, Z. Zhang, B. Shen, B. Kang, S. R. P. Silva and L. Wang, High-efficiency planar heterojunction perovskite solar cell produced by using 4-morpholine ethane sulfonic acid sodium salt doped $SnO_2$, *J. Colloid Interface Sci.*, 2022, **609**, 547–556.

22 P. Wang, B. Chen, R. Li, S. Wang, N. Ren, Y. Li, S. Mazumdar, B. Shi, Y. Zhao and X. Zhang, Cobalt Chloride Hexahydrate Assisted in Reducing Energy Loss in Perovskite Solar Cells with Record Open-Circuit Voltage of 1.20 V, *ACS Energy Lett.*, 2021, **6**(6), 2121–2128.

23 T. Bu, J. Li, F. Zheng, W. Chen, X. Wen, Z. Ku, Y. Peng, J. Zhong, Y.-B. Cheng and F. Huang, Universal passivation strategy to slot-die printed $SnO_2$ for hysteresis-free efficient flexible perovskite solar module, *Nat. Commun.*, 2018, **9**, 4609.

24 Z. Yang, Y. Deng, X. Zhang, S. Wang, H. Chen, S. Yang, J. Khurgin, N. X. Fang, X. Zhang and R. Ma, High-Performance Single-Crystalline Perovskite Thin-Film Photodetector, *Adv. Mater.*, 2018, **30**(8), 1704333.

25 X. Guo, J. Du, Z. Lin, J. Su, L. Feng, J. Zhang, Y. Hao and J. Chang, Enhanced efficiency and stability of planar perovskite solar cells using $SnO_2$:$InCl_3$ electron transport layer through synergetic doping and passivation approaches, *Chem. Eng. J.*, 2021, **407**, 127997.

26 Y. Zhao, L. Gao, Q. Wang, Q. Zhang, X. Yang, J. Zhu, H. Huang, J. Duan and Q. Tang, Reinforced $SnO_2$ tensile-strength and "buffer-spring" interfaces for efficient inorganic perovskite solar cells, *Carbon Energy*, 2024, **6**(6), e468.

27 Q. Feng and G. Nan, How Do A-Site Cations Regulate Trap States at Defective Surfaces of Lead Iodide Perovskites?, *J. Phys. Chem. Lett.*, 2022, **13**(21), 4831–4839.

28 Y. Rui, T. Li, B. Li, Y. Wang and P. Mueller-Buschbaum, Two-dimensional $SnS_2$ nanosheets as electron transport and interfacial layers enable efficient perovskite solar cells, *J. Mater. Chem. C*, 2022, **10**(34), 12392–12401.

29 J. Sun, Y. Gu, Y. Lu, J. Hu, T. Chen, C. Zhu and P. Luo, Synergistic strategy of rubidium chloride regulated $SnO_2$ and 4-butyl-benzylammonium iodide passivated MAxFA1-xPbI3 for efficient mixed-cation perovskite solar cells, *Chem. Eng. J.*, 2023, **468**, 143722.

30 L. Xiong, Y. Guo, J. Wen, H. Liu, G. Yang, P. Qin and G. Fang, Review on the Application of $SnO_2$ in Perovskite Solar Cells, *Adv. Funct. Mater.*, 2018, **28**(35), 1802757.

31 S. Das, S. Senapati, G. K. Pradhan, S. Varadharajanperumal and R. Naik, A Facile Microwave-Assisted Nanoflower-to-Nanosphere Morphology Tuning of CuSe1–xTe1+x for Optoelectronic and Dielectric Applications, *ACS Appl. Nano Mater.*, 2023, **6**(7), 5298–5312.

32 S. Giri, P. C. Kumar, S. Supriya, D. Alagarasan and R. Naik, Enhanced photodetectivity and responsivity in In10Se70Te15Bi5 film by time-dependent laser irradiation for photodetector applications, *RSC Adv.*, 2025, **15**(55), 46821–46837.

33 J. Liu, S. Li, S. Liu, Y. Chu, T. Ye, C. Qiu, Z. Qiu, X. Wang, Y. Wang, Y. Su, Y. Hu, Y. Rong, A. Mei and H. Han, Oxygen Vacancy Management for High-Temperature Mesoporous $SnO_2$ Electron Transport Layers in Printable Perovskite Solar Cells, *Angew. Chem., Int. Ed.*, 2022, **61**(26), e202202012.

34 Y. Ai, W. Liu, C. Shou, J. Yan, N. Li, Z. Yang, W. Song, B. Yan, J. Sheng and J. Ye, $SnO_2$ surface defects tuned by $(NH_4)_2S$ for high-efficiency perovskite solar cells, *Sol. Energy*, 2019, **194**, 541–547.

35 X. Tao, H. Chen, Y. Zhou, Q. Peng and Y. Ouyang, The formation energy and interaction energy of point defects in ZrC, *J. Nucl. Mater.*, 2021, **557**, 153235.

36 Z. Wang, M. A. Kamarudin, N. C. Huey, F. Yang, M. Pandey, G. Kapil, T. Ma and S. Hayase, Interfacial Sulfur Functionalization Anchoring $SnO_2$ and $CH_3NH_3PbI_3$ for Enhanced Stability and Trap Passivation in Perovskite Solar Cells, *Chemsuschem*, 2018, **11**(22), 3941–3948.

37 S. B. Hong, S. Kim and H. W. Choi, Improved Performance of Perovskite Deep-Ultraviolet Photodetector Using FAPb(I/Br)3 as Light Absorption Layer, *Coatings*, 2023, **13**(2), 341.

38 D. J. Shin, S. Kim and H. W. Choi, Effect of Methylammonium Iodide (MACl) on MAPbI3-Based Perovskite UV-C Photodetectors, *Appl. Sci.*, 2024, **14**(14), 6223.

39 W. Qu, S. Weng, L. Zhang, M. Sun, B. Liu, W. Du and Y. Zhang, Self-powered ultraviolet–visible–near infrared perovskite/silicon hybrid photodetectors based on a novel Si/SnO2/MAPbI3/MoO3 heterostructure, *Appl. Phys. Express*, 2020, **13**(12), 121001.

40 W. Song, J. Lv, J. Li, X. Huang, H. Duan, H. Qin, S. Ma, J. Wei, X. He and Z. Li, Picowatt-Sensitive and Air-Stable Heterojunction UV Photodetectors Enabled by Large-Grained CsCu2I3 Film via Microgap Thermal Sublimation, *ACS Photonics*, 2025, **12**(8), 4478–4488.

41 Y. Peng, D. Jiang, M. Zhao, Y. Duan, H. Wei, H. Li, Q. Liang and S. Wang, High-performance UV-visible photodetectors based on ZnO/perovskite heterostructures, *J. Alloys Compd.*, 2023, **965**, 171372.

42 H. Zhou, J. Mei, M. Xue, Z. Song and H. Wang, High-Stability, Self-Powered Perovskite Photodetector Based on a CH3NH3PbI3/GaN Heterojunction with C60 as an Electron Transport Layer, *J. Phys. Chem. C*, 2017, **121**(39), 21541–21545.

43 Y. Yuan, H. Tao, H. Wang, J. Liu, Y. Zhang, Q. Fu, H. Zhao, T. Di, H. Long and S. Yao, The effect of UVO treatment on TiO2-MAPbI3 heterostructure photodetector prepared in air atmosphere, *Mater. Sci. Semicond. Process.*, 2024, **172**, 108079.

44 T. Li, H. Wu, Y. Hao, F. Ma, P. Zhu, Z. Li, F. Li, J. Yu, M. Liu, C. Lei and T. Liang, High-Performance Broadband

Photodetectors Combining Perovskite and Organic Bulk Heterojunction Bifunctional Layers, *Crystals*, 2024, **14**(10), 868.

45 X. Xu, Z. Liu, W. Chen, Y. Chen, W. He and Y. Peng, Heteropoly Blue Modified SnO2 for Highly Efficient Perovskite-Based Photodetectors, *ACS Appl. Energy Mater.*, 2025, **8**(9), 6112–6120.

46 S. Fang and Y. H. Hu, Thermo-photo catalysis: a whole greater than the sum of its parts, *Chem. Soc. Rev.*, 2022, **51**(9), 3609–3647.